Electrochimica Acta 405 (2022) 139810

Contents lists available at ScienceDirect

Electrochimica Acta

journal homepage: www.elsevier.com/locate/electacta

Mechanistic understanding of pH effects on the oxygen evolution reaction

Julie C. Fornaciari[a,b,1], Lien-Chun Weng[a,b,1], Shaun M. Alia[c], Cheng Zhan[d], Tuan Anh Pham[d], Alexis T. Bell[b], Tadashi Ogitsu[d], Nemanja Danilovic[a], Adam Z. Weber[a,*]

[a] Energy Storage and Distributed Resources Division, Lawrence Berkeley National Laboratory, Berkeley, CA 94720
[b] Department of Chemical and Biomolecular Engineering, University of California Berkeley, Berkeley CA 94720
[c] Chemistry and Nanoscience Center, National Renewable Energy Laboratory, Golden, Colorado 80401
[d] Quantum Simulations Group, Lawrence Livermore National Laboratory, Livermore, California 94551

ARTICLE INFO

Article history:
Received 19 September 2021
Revised 1 December 2021
Accepted 29 December 2021
Available online 31 December 2021

Keywords:
Microkinetics
Electrochemistry
Oxygen evolution reaction

ABSTRACT

The oxygen-evolution reaction (OER) is pivotal in many energy-conversion technologies as it is an important counter reaction to others that convert stable chemicals to higher-value products using electrochemistry. The local microenvironment and pH for the anode OER can vary from acidic to neutral to alkaline depending on the system being explored, making definitive mechanistic insights difficult. In this paper, we couple experiments, first-principles calculations based on density functional theory, microkinetics, and transport modeling to explore the entire pH range of the OER. At low current densities, neutral pH values unexpectedly perform better than the acidic and alkaline conditions, and this trend is reversed at higher current densities ($>$ 20 mA cm^{-2}). Using multiscale modeling, this switch is rationalized by a change from a dual-reaction mechanism to a single rate-determining step. The model also shows how the alkaline reaction rates dominate in the middle to high pH range. Furthermore, we explore that the local pH for near-neutral conditions is much different (*e.g.*, 2.4 at the reaction surface vs. 9 in the bulk) than the pH extremes, demonstrating the criticality that transport phenomena plays in kinetic activity.

© 2022 The Authors. Published by Elsevier Ltd.
This is an open access article under the CC BY license (http://creativecommons.org/licenses/by/4.0/)

1. Introduction

As renewable-energy generation grows, it is predicted that there will be an excess of inexpensive electrical energy, and storing this excess electricity in chemical bonds provides a viable pathway for long-duration storage and decarbonizing various energy sectors [1–5].The key and often limiting reaction in this process is the oxygen-evolution reaction (OER), which is required as water is the traditional proton source. The OER occurs in multiple environments across the pH range depending on the specific cell and applications [6–12]. Of particular interest is the near-neutral range as it avoids corrosive solutions (strong acids and bases), and is compatible with photoelectrochemical water splitting among other technologies [1, 13-16]. Although the OER has been studied in various pH conditions, there is still missing mechanistic understanding of how it proceeds, especially when not under highly acidic or alkaline conditions.

The OER is shown in acidic and alkaline conditions in Eqs. (1) and (2), respectively.

$$2H_2O \rightarrow O_2 + 4H^+ + 4e^- \quad 1.23 \text{ vs. SHE} \tag{1}$$

$$4HO^- \rightarrow O_2 + 2H_2O + 4e^- \quad 0.40 \text{ vs. SHE} \tag{2}$$

Electrochemical and photoelectrochemical systems have studied the OER by investigating catalyst nanoparticles (films and single- and poly- crystals) [7,9,10,17,18] in half-cell (rotating disk electrode) [10,11,19,20] or full-cell (membrane electrode) experiments [21,22]. These types of studies are used to elucidate the effect of either the electrocatalyst or the electrolyte composition (identity of cations, anions, and pH) on the OER rate. Conventionally, product or reactant transport limitations to or from the reaction site are assumed to be negligible, and experiments are typically conducted at extreme pHs (low and high), where there is significant concentration of either H^+ and OH^-. However, there is a dearth of work at near-neutral pHs, which are especially relevant to photoelectrochemical water splitting and electrosynthesis.

To understand the OER mechanism, density functional theory (DFT) has often been used to determine reaction free energies for

* Corresponding author.
E-mail address: azweber@lbl.gov (A.Z. Weber).
[1] Equal Contributions.

https://doi.org/10.1016/j.electacta.2021.139810
0013-4686/© 2022 The Authors. Published by Elsevier Ltd. This is an open access article under the CC BY license (http://creativecommons.org/licenses/by/4.0/)

different surface states, which provides insight into surface coverage and transition states [23,24]. DFT calculations provide information of reactions on specific catalyst surfaces, but, due to computational complexity, are carried out for small system sizes, ideal crystals and conditions that might not adequately represent experimental conditions. In addition, existing DFT calculations largely focus on providing the energy and free energy between different states, while neglecting other important effects, such as adsorbate coverages by different species at the electrode.

Microkinetic analysis can be used to identify limiting steps and evaluate mechanisms. This approach can be combined with DFT and thermodynamic analyses tuned by experimental data for the energy-barrier predictions, since direct measurements of these multi-step processes remains inaccessible. Rates of reaction and surface coverages can be determined by microkinetic analysis and several studies have shown how the rates change with potential and, in some cases, with pH [12,25]. The recent study by Nishimoto *et al.* [25] examined how the kinetics change over the entire pH range based on an in-depth kinetic analysis for the OER using an IrO_x electrocatalyst. Their work suggests the O–O bond formation step is the rate-determining step and examines how anode potential impacts the kinetics for acidic, alkaline, and neutral conditions up to a current density of 20 mA cm^{-2} [25]. While many studies have shown the fundamental interactions of adsorbates and ions on catalyst surfaces, based upon theory, modeling, and experiments, the effects of transport are often neglected in these studies [12,25]. Furthermore, the length scales involved in the OER from the ions approaching the surface and undergoing reaction are very different and concomitantly modeled with different approaches; minimal work has been done to bridge the gap between these phenomena, particularly in the neutral to near-neutral range. An initial effort towards this end demonstrated the importance of transport phenomena, in that it shifted the dominant reaction pathway under operation from the lowest energy one predicted by the reaction barriers alone [26]. For the mid-pH range, transport is expected to perhaps be more important due to the lack of high proton and hydroxide concentrations in the bulk, especially at higher current densities.

In this study, we investigate the OER under controlled pH using a rotating-disk electrode half-cell and interpret the results using a microkinetic model, as illustrated in Fig. 1. Free energies of the different states were calculated using DFT and the barriers from combined thermodynamic, DFT, and experimental studies. The modeling also examines the effects of ionic transport, to obtain a more complete picture of the OER for different pH regimes. The results of this work provide insight into the effects of kinetics and transport and data of the OER across the entire pH range that will aid the design of better electrolytic and photoelectrolytic devices.

2. Experimental

2.1. Rotating-disk-electrode measurements

The iridium oxide catalyst (Alfa Aesar) were suspended in a solvent mixture to make an ink and deposited onto a ChangeDisk Tip (Pine Research Instrumentation) for electrochemical testing. The inks were composed of 3.49 mg catalyst (metal basis) in 7.6 ml of 18.2 mΩ distilled, deionized water (<5 ppb organic carbon content, TOC), 2.4 ml isopropyl alcohol, and 40 μl Nafion ionomer (5 wt%, Sigma-Aldrich). The catalyst was first added to the water and IPA, placed in an ice bath for 5 min, and then the ionomer dispersion was added. The ink was horn sonicated for 30 s, bath sonicated for 20 min, and then horn sonicated for another 30 s. 10 μl of ink was then deposited on the electrode tip rotating at 100 RPM to achieve a catalyst loading of 17.8 μg_M cm^{-2} with an ionomer to catalyst mass ratio of 0.1 μg_{Nafion} $mg_{Catalyst}{}^{-1}$, which was shown previously to produce reasonable inks and RDE activities for nanoparticle catalysts intended for PEM fuel cells and electrolyzers [18,19]. The speed was then increased to 700 RPM and the electrodes were allowed to dry in air at room temperature.

Prior to testing, the electrodes were conditioned by cycling (50 cycles) the working electrode in the potential range 1.2 to 1.8 V vs. RHE at 100 mV s^{-1} and a rotation speed of 2500 rpm in a nitrogen-saturated electrolyte. Activities were taken during linear-sweep voltammograms (LSVs) at 20 mV s^{-1} and 2500 rpm, with one voltammogram taken to cover the kinetic region (1.2 to 1.65 V) and another to cover the full potential range (1.2 to 2.0 V). Voltammograms were corrected for internal resistance (reference electrode Lugin tip to working electrode) during the measurement as opposed to during post-processing. These values were taken with a built-in current interrupter at 1.65 V.

Rotating-disk-electrode (RDE) testing was conducted using a three-electrode system in a polytetrafluoroethylene cell (Pine Research Instrumentation). The cell was equipped with a catalyst-coated gold working electrode (or polycrystalline Ir electrode), a gold wire/mesh counter electrode, and a reversible hydrogen reference electrode. The working electrode, which has a surface area of 0.196 cm^2, was rotated with a modulated speed rotator (Pine Research Instrumentation) and electrochemical measurements were taken with an Autolab potentiostat (Eco Chemie, Metrohm Autolab B.V.). The electrolytes that were tested consisted of perchloric acid (ACS grade), potassium perchlorate (Sigma Aldrich), and potassium hydroxide (Suprapur, EMDMillipore). The electrolytes were titrated to reach desired pH values, ranging from 1 to 13, and were used to avoid contaminants and other interference effects associated with buffers [27]. pH and electrolyte conductivity (shown in Table S1 and Figure S2) were continually monitored and logged to tune experimental conditions and assess electrolyte changes during individual experiments. The magnitude of bulk pH changes depended on the initial electrolyte pH and experiment parameters and could be severe with repeated voltammograms to higher current density. When focusing on the kinetic region (up to 1.65 V) at an initial pH 7, the bulk pH could change up to 0.3 during the evaluation. At high or low bulk pH (1, 13), the change was negligible.

Table 1
The mechanism steps and the net reaction rate for all eight steps. Acidic steps shown by reactions 1 thru 4 (Eqs. 3 thru 6) and alkaline steps shown by reactions 5 thru 8 (Eqs. 7 thru 10).

Mechanism Step	Net Reaction Rate	
$^*OH \leftrightarrow {}^*O + H^+ + e^-$	$r_1 = k_{f1}\theta_{*OH} - k_{r1}a_{H^+}\theta_{*O}$	(3)
$H_2O + {}^*O \leftrightarrow {}^*OOH + H^+ + e^-$	$r_2 = k_{f2}a_0\theta_{*O} - k_{r2}a_{H^+}\theta_{*OOH}$	(4)
$^*OOH \leftrightarrow {}^* + O_2 + H^+ + e^-$	$r_3 = k_{f3}\theta_{*OOH} - k_{r3}a_{H^+}a_{O_2}\theta_*$	(5)
$H_2O + {}^* \leftrightarrow {}^*OH + H^+ + e^-$	$r_4 = k_{f4}a_0\theta_* - k_{r4}a_{H^+}\theta_{*OH}$	(6)
$OH^- + {}^*OH \leftrightarrow {}^*O + H_2O + e^-$	$r_5 = k_{f5}a_{OH^-}\theta_{*OH} - k_{r5}a_0\theta_{*O}$	(7)
$^*O + OH^- \leftrightarrow {}^*OOH + e^-$	$r_6 = k_{f6}a_{OH^-}\theta_{*O} - k_{r6}\theta_{*OOH}$	(8)
$^*OOH + OH^- \leftrightarrow {}^* + H_2O + O_2 + e^-$	$r_7 = k_{f7}a_{OH^-}\theta_{*OOH} - k_{r7}a_0a_{O_2}\theta_*$	(9)
$OH^- + {}^* \leftrightarrow {}^*OH + e^-$	$r_8 = k_{f8}a_{OH^-}\theta_* - k_{r8}\theta_{*OH}$	(10)

3. Theoretical

3.1. Microkinetics

Table 1 shows the eight-step kinetic mechanism used for all simulations. The reaction mechanism is based on Nørskov's OER mechanism for both H^+ and OH^-elementary steps [28,29]. All eight steps were considered simultaneously throughout the potential range (1.2 – 2.0 V vs. RHE) and the pH range (0 to 14). In equations 3 thru 10, the net rate of formation of species i (r_i) is defined by the differences in the rates of the forward and reverse reactions for each of the eight elementary steps. The activity for water (a_0) is assumed to be 1 and the activity for the H^+ (a_{H^+})

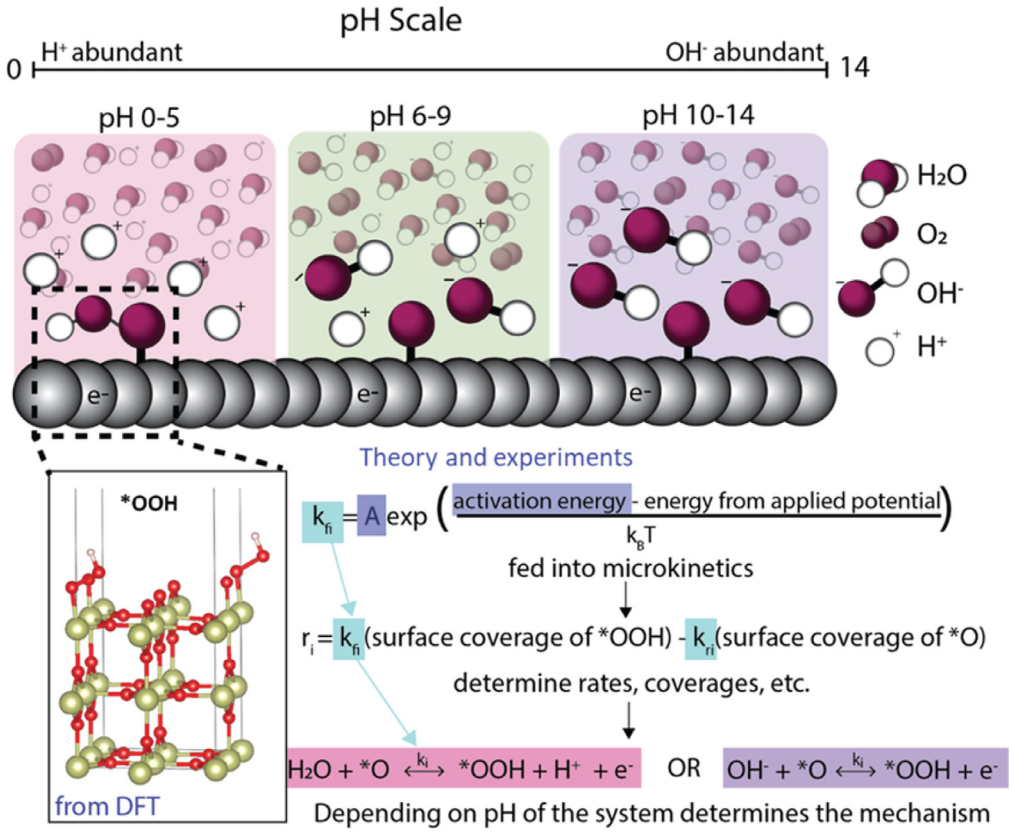

Fig. 1. A schematic showing the catalyst and the active species for the various pH conditions (counterions are ignored). The structure of the catalyst is determined by DFT and then is fed into the microkinetics, qualitatively depicted here. The preexponential factor and activation energy was calculated based on theory and experimental data. [29].

is calculated using the bulk pH of the given simulation. The activity for OH^- (a_{OH^-}) was calculated based on the water dissociation constant, using the standard Gibbs free energy of reaction, and the activity for H^+.

The surfaces coverages were calculated by

$$\frac{\partial \theta_*}{\partial t} = -r_4 + r_3 - r_8 + r_7 \tag{11}$$

$$\frac{\partial \theta_{*OH}}{\partial t} = r_4 - r_1 + r_8 - r_5 \tag{12}$$

$$\frac{\partial \theta_{*O}}{\partial t} = r_1 - r_2 + r_5 - r_6 \tag{13}$$

$$\theta_* + \theta_{*OH} + \theta_{*O} + \theta_{*OOH} = 1 \tag{14}$$

where θ_{*OH}, θ_{*O}, θ_{*OOH} and θ_* denote surface adsorbed species or empty sites. The initial conditions for these ordinary differential equations are $\theta_* = 1$, and the activity of oxygen (a_{O_2}) is zero, as there is no reaction at the $t = 0$.

Rate coefficients, free energies, and activation energies are required to define the system. The forward reaction rate coefficients in Table 1 can be written as

$$k_{fi} = A \exp\left(\frac{\Delta E_{\ 0V} - \beta n_i eV}{k_B T}\right) \tag{15}$$

where A is the pre-exponential factor, β is the transfer coefficient, k_B is the Boltzmann constant, T is the absolute temperature, n_i is the number of electrons in the reaction, eV is the applied voltage, and $\Delta E_{\ 0V}$ is the activation energy ($\Delta E_{\ 0V}$) assuming 0 V free-energy change. The transfer coefficient describes the activation energy dependence on applied potential, which in theory can be obtained from first-principles simulations. However, in these simulations, the various rate parameters for each reaction were obtained from an analytical model developed by Exner *et al.* that combines DFT calculation and experimental data [30], and the reaction free energies were computed by first-principles thermodynamics as described below.

The reverse reaction rate coefficient is obtained from our DFT calculation and the equilibrium constant,

$$\frac{k_{f_i}}{k_{r_i}} = K_i = \exp\left(\frac{\Delta G_{rxn,\ 0V} - n_i eV}{k_B T}\right), \tag{16}$$

where $\Delta G_{rxn,\ 0V}$ is the Gibbs free energy of reaction at 0 V calculated using DFT.

To solve the system of equations, the reaction rate constants Eqs. (15) and ((16)) were substituted into the reaction rate expressions (equations 3 thru 10) and then into the differential equations for species' coverage (equations 11 thru 14), where were solved simultaneously using MATLAB to predict the current density for the OER given the bulk pH value, the calculated rate constants, and the operating potential.

3.2. Density functional theory

As noted above and in Fig. 1, the various reaction step free energies are derived from DFT simulations, with the rate constants taken from the combined experimental and theoretical study of Exner et al. [30]. All of the DFT calculations were performed using the Quantum Espresso code [31]. The IrO_2(110) surface was modeled using a 2 × 1 orthorhombic cell with the lattice parameter of a = 6.34 Å, b = 6.38 Å, c = 40.00 Å and five Ir atomic lay-

ers (Fig. 1 inset, SI Figure S3). In addition, the vacuum slab thickness was set to 20 Å to avoid the periodic interaction along the *z* axis. The Perdew-Burke-Ernzerhof the exchange-correlation functional with van der Waals corrections proposed by Grimme (DFT-D2) was used for all DFT calculations [32,33]. A plane-wave basis set was used to expand the wavefunction and electron density with energy cutoffs of 40 and 320 Ry, respectively. Spin polarization along the *z* direction was included in all the simulations. We used a 6 × 6 × 1 k-mesh for Brillouin zone sampling. The convergence criteria of structure relaxation and single point calculation were set as 10^{-3} Ry/bohr and 10^{-6} Ry, respectively.

Thermodynamics of OER for the four intermediates involved in the OER were computed using a four proton-coupled-electron-transfer (PCET) reaction process, shown in Eqs. (17)-(20), where "*" refers to the oxygen vacancy on the oxide surface. The voltage-dependent reaction free energy ($\Delta G(U)$) can be computed using the computational hydrogen electrode method (CHE) [29],

$$\Delta G_1 = G(^*\mathrm{O}) + \frac{1}{2}G(\mathrm{H_2}) - G(^*\mathrm{OH}) - eU \quad (17)$$

$$\Delta G_2 = G(^*\mathrm{OOH}) + \frac{1}{2}G(\mathrm{H_2}) - G(^*\mathrm{O}) - G(\mathrm{H_2O}) - eU \quad (18)$$

$$\Delta G_3 = G(^*) + G(\mathrm{O_2}) + \frac{1}{2}G(\mathrm{H_2}) - G(^*\mathrm{OOH}) - eU \quad (19)$$

$$\Delta G_4 = G(^*\mathrm{OH}) + \frac{1}{2}G(\mathrm{H_2}) - G(^*) - G(\mathrm{H_2O}) - eU \quad (20)$$

where *G* is the free energy of individual species or surface site, and *U* is the applied electrode potential referenced to the reversible hydrogen electrode (RHE). The free energy of each reaction intermediate was obtained from the DFT total energy and thermal energy correction:

$$G = E_{elec} + E_{ZPE} + \int C_p \mathrm{d}T - TS \quad (21)$$

where E_{elec} is the DFT total energy and E_{ZPE} is the zero-point-energy correction, which are directly available by performing single point calculation and normal mode calculation. The latter two terms are the thermal energy correction and the entropy contributions, respectively. Here, the heat capacity can be obtained by either using a simple ideal gas model, such as monoatomic or diatomic molecule ansatz, or by using the standard thermodynamics database. The entropy contribution can also be obtained in the similar ways, noting that this is zero order gas-phase prediction that ignores specific solvation effects. In our work, the thermal energy correction and entropy of H_2 and H_2O was introduced from early study by Peterson *et al.* [34]. We note that the free energy of single oxygen molecule O_2 was computed by the standard formation free energy of H_2O (−2.46 eV) at the standard condition and $G(H_2)$. The calculated reaction free energies (U = 0.00 V vs. RHE) of steps 1 thru 4 (see Table 1) are listed in Table S2.

Beyond the thermodynamics of OER intermediates, we adopted the strategy proposed by Exner et al., to construct the full free energy diagram of OER that also includes information of transition states (TS) [30]. Specifically, the number of electrons transferred and TS free energy of the rate-determining reaction step were determined from experimental Tafel plots and exchange current density, respectively [30]. They are then combined with DFT-based surface phase diagram to determine the initial state of OER reaction (Figure S4) and thermodynamics of reaction intermediates to construct the OER free energy diagram at different potentials (Figure S4 and S5). As noted in [30], such an approach is validated by comparison to previous experimental data.

3.3. Transport model

To simulate mass-transport phenomena within the RDE, a two-dimensional, transient, isothermal transport model was used. The model domain consists of the electrolyte with a boundary of bulk conditions and a rotating disk as shown in Figure S6a. The governing equations consists of the species (H^+, O_2, ClO_4^-, K^+, OH^-) mass balances with the Nernst-Planck equation describing the various transport equations. For the convective velocity to the rotating disk, in both the *z* and *r* directions, a von Karmen and Cochran expression is used. Finally, the rate of reaction for the OER is given based on the local current density as determined from the microkinetic model. All governing equations and associated boundary conditions are in Tables S3 and S4. The model was solved using COMSOL Multiphysics.

4. Results and discussion

The OER performance via LSV was evaluated across the pH range on commercial IrO_2 nanoparticles as shown in Fig. 2. These half-cell experiments were accomplished while holding the bulk pH constant, which was achieved through titrating the electrolyte. It should be noted that the bulk electrolyte conditions, which are monitored through titration, are taken as the RHE baseline. In the acidic and neutral range, Figs. 2a and b, increasing pH seemingly results in worse performance in terms of a lower current density at a given potential. For higher pH shown in Fig. 2c, however, the trend is not as monotonic. Fig. 2d shows the comparison more easily in terms of overlaying three different polarization curves at a neutral (pH = 9), acidic (pH = 1), and alkaline (pH = 13) pH. From that figure, it is readily apparent that at low current densities the more neutral pH demonstrates more current for a given potential, although this better performance disappears at higher current density, where the high and low pH yield more current than the pH = 9 case. This trend of superior performance of Ir-based catalysts for the OER under conditions of intermediate pH was also observed for polycrystalline Ir and Ir-metal nanoparticles (see Figure S1).

Fig. 3 provides a different perspective on this unexpected outcome by displaying the experimental and the simulation results for four different scenarios: (a) low current density, (b) high current density, (c) low potential, (d) high potential. Interestingly, in all of curves, the performance (either current density at fixed potential or potential at fixed current density) demonstrate a seeming discontinuity around pH = 6. This result is particularly seen when examining performance at fixed potential (Fig. 3c, d) where the current density initially decreases with increasing pH, then exhibits an increase around pH = 6 followed by a decrease again. As discussed later, this pH results in ideal conditions for both acidic and alkaline reactions mechanisms to occur. As shown in Fig. 3a, at 2 mA cm^{-2}, and in Fig. 3c, it is clear that the more neutral pH range demonstrates increased performance compared to either pH extreme. The seemingly large increase in performance at pH 6 is notable, and was consistent throughout these experiments (see Figure S1). Further experiments, perhaps with buffers, is required to understand fully the reasons for this value, which may stem from the sensitivity to logarithmic nature of pH and near neutral conditions. However, at higher current density (Fig. 3b) or higher potential (Fig. 3d), this trend is reversed with the extreme pH's outperforming the middle pH range, which is somewhat consistent with literature [35, 36], although in that case the alkaline provided the highest current density for a given potential. This discrepancy can perhaps be related to the way in which those systems used buffers instead of titration to maintain pH, as is done here. Although beyond the scope of the current study, the use of buffers could lessen the impact of the pH changes during operation, al-

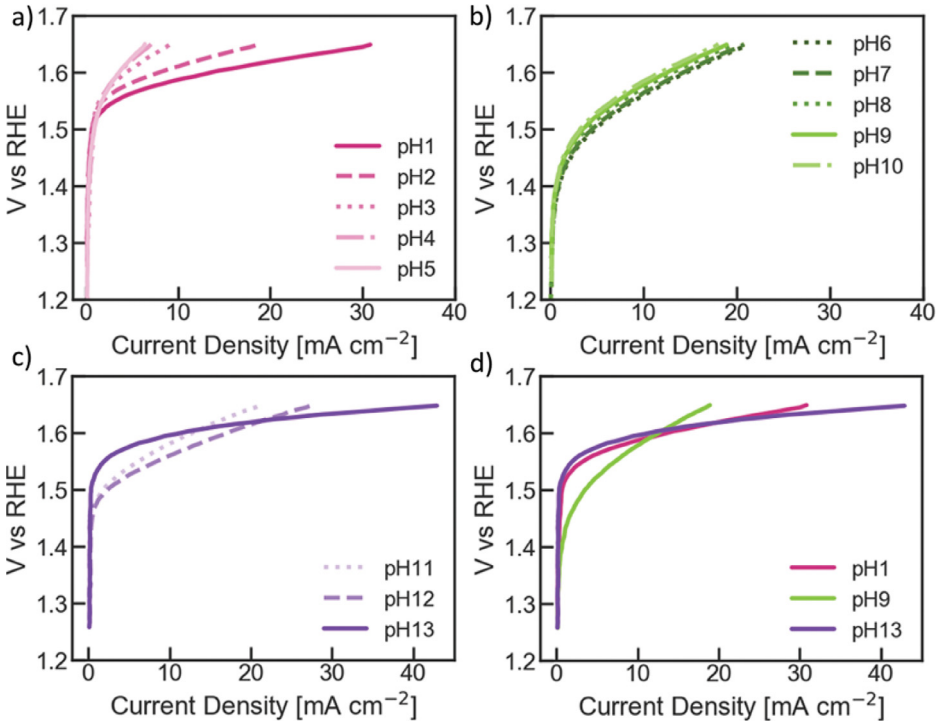

Fig. 2. Linear-sweep voltammograms shown for (a) acidic pH (1 thru 5), (b) neutral to near neutral pH (6 thru 10), and (c) alkaline pH (11 thru 13). The most acidic and alkaline pH's, 1 and 13, respectively, and pH 9 are shown in comparison (d) and are investigated as representative cases in the modeling sections throughout this paper.

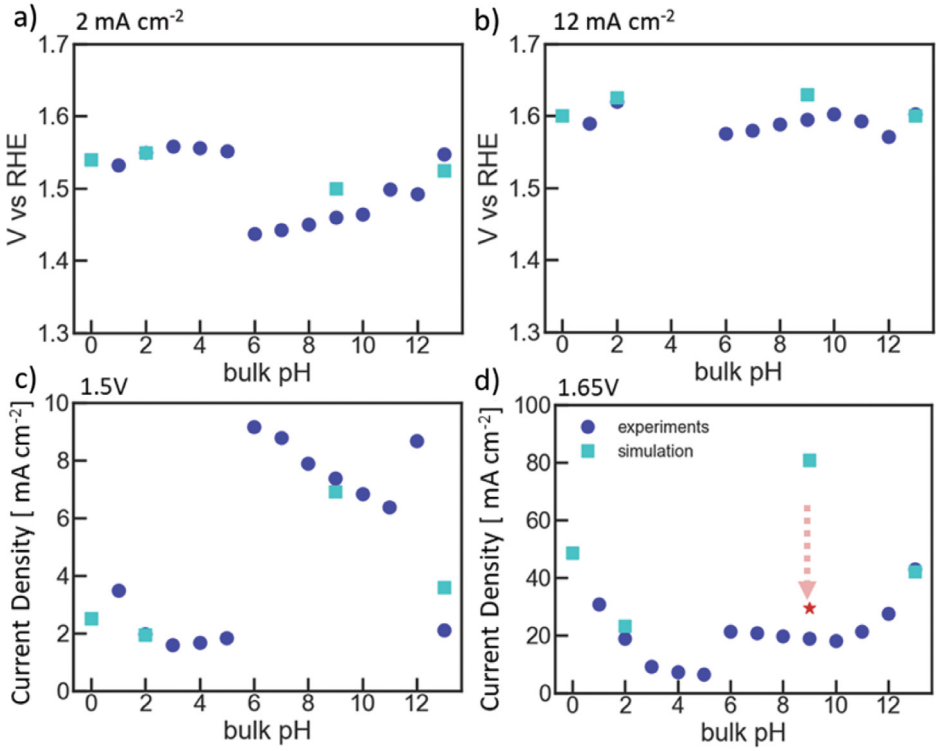

Fig. 3. Oxygen evolution overpotential as a function of bulk pH, for IrO_2 nanoparticles from experiments (circles) and simulations (squares). The potentials were reported at current densities of (a) 2 mA cm^{-2} and (b) 12 mA cm^{-2}. The current densities were reported at corresponding voltages of (c) 1.5 V and (d) 1.65 V. The pH's ran in the simulation are pH 0, 2, 9, and 13. The red star indicates the pH at the surface of the electrode, 2.34, determined by the transport model, when the bulk pH is 9.

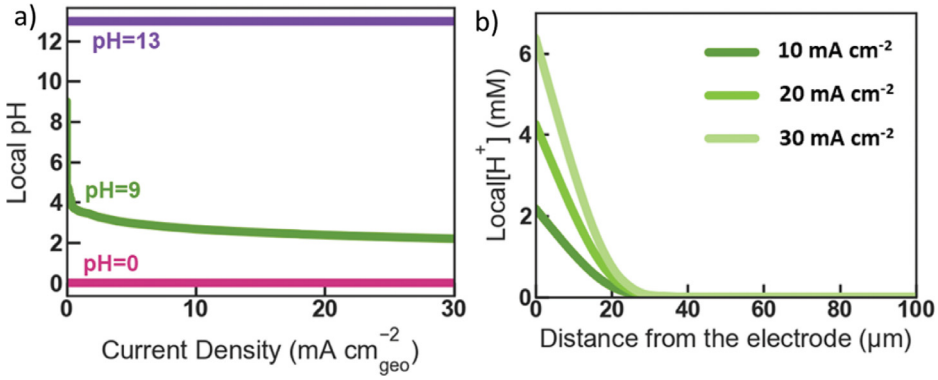

Fig. 4. (a) The local pH as a function of current density for pH 0, 9 and 13. (b) The local proton concentration as a function of distance from the electrode at pH 9.

though this will depend on device design, buffer concentrations, current density, etc.; surface pH would still vary due to interplay between buffer reaction rates and capacities and generation rates, as seen in simulations for CO_2 electrolysis in RDEs [37]. Finally, it should be noted that the low current-density comparison (Fig. 3a, c) aligns nicely with the expected low current densities and shows the need for near neutral pH (to avoid degradation) in photoelectrochemical water-splitting and related solar-fuel technologies [38].

To further interpret the data, simulations were carried out for several different pHs at low and high current densities (applied potentials). As shown in Fig. 3, decent agreement was realized with the model except for pH 9 at 1.65 V (>20 mA cm^{-2}) (see Fig. 3d). To ascertain the cause of the discrepancy, a transport model of the RDE was run to explore how the local pH at the reaction site varies as a function of bulk pH, especially since the bulk pH was held constant by titration. As shown in Fig. 4a, the local pH at 13 and 0 is the same as the bulk, but at pH 9 it deviates quite significantly, changing by orders of magnitude as the current density (applied potential) increases. Fig. 4b shows that virtually all of this change occurs within the mass-transfer boundary layer near the anode, which can be varied to modulate the pH (see Figure S7). Accounting for this concentration-polarization effect shifts the simulation at pH 9 to be in better accord with the experimental data, as shown in the translated point in Fig. 3d following the arrow from the square to the star.

To understand the trends in Figs. 2 and 3, the microkinetic simulation results are used to ascertain the rate-determining step(s) via a perturbation analysis. The analysis entails perturbing each individual reaction rate constant by a small amount (~0.1%) and calculating the net change in the overall reaction rate or current density (see Figure S8 for the individual reaction rate plots). Fig. 5a-c shows the results from the perturbation analysis at three different pHs: 0, 9, and 13, respectively. For pH 0, two different rate-determining steps are identified at low applied voltages, namely *OOH formation (eq. 4) and O_2 formation (eq. 5). However, at higher potentials (> 1.6 V), only one rate determining step occurs, *OOH formation (eq. 4), which is related to the change in the surface coverages at higher potential, which agrees with previous studies [30,39]. For pH 13, shown in Fig. 5c, the rate-determining step is clearly *OOH formation (eq. 8). It is interesting to note that this rate-determining step persists to relatively low pH, owing perhaps to the use of converting OH^- and not needing to break a H–O-H bond in water. We do note that to agree with the alkaline pathways, the DFT predicted activation energy had to be increased from that of Exner *et al.* [30], as noted in Figure S9 for the example case of pH 13, but was within the DFT error. This difference in activation energy may be due to the underlying ideal IrO_2 (110) surface used for the DFT calculations, as opposed to polycrystalline nanoparticle IrO_2 used in the experiments. The changes in the Gibbs free energy along the reaction pathway for the acidic and alkaline mechanisms presented in Table 1 are given in Fig. 6, and comprise the main drivers for the results in Fig. 5. Together, these results help explain the differences in Fig. 3.

At neutral pH, both acidic and alkaline mechanisms may occur, with the alkaline pathway slightly dominating due to the lower barrier from the DFT for the second step (Eq. 4 and 8) as shown in Fig. 5b and Figure S10 from perturbation analysis and extent of reaction analysis, respectively. This finding also helps to rationalize the enhanced low current-density performance at neutral pHs. It is also consistent with the change in Tafel slope at middle pHs (see Figure S11), which suggest a mechanistic change is occurring. Although the Tafel slope does increase for the middle pH range, the onset potential is lower than at the extreme pHs, thereby agreeing with the above rate-limiting step changes. Furthermore, at low overpotential for near-neutral pH, it is also believed that in addition to having both types of charge carriers, there may also be altered adsorption/desorption, as suggested by the increased response at low potential (< 1.5 V) in the cyclic voltammograms (see Figure S12) and in Fig. 5d. This influence goes away at higher current densities where the local microenvironment changes to much more acidic. This increased response may result in differences in intermediate binding, the rate-determining step, or transition-state energy, and are not reflected in the DFT or microkinetics herein, and to verify such surface coverages *operando* requires careful ambient pressure X-ray photoelectron spectroscopy measurements in conjunction with more detailed theoretical calculations [40–42] in which a more detailed DFT simulation is required since the predicted surface Pourbaix does not show substantial coverage differences as a function of pH (see Figure S4a). Finally, it should be noted that for these comparisons, the local pH is being examined and as mentioned above, deviates to lower pH values for near neutral bulk pH due to transport phenomena.

5. Summary

In this paper, DFT, microkinetics, and transport modeling, show a multiscale picture of the oxygen-evolution reaction (OER) over a large pH range. This analysis provides informative findings for acidic and alkaline electrolyzers and near-neutral photoelectrochemical systems at operating current densities (<100 mA cm^{-2}). For near-neutral pH systems at low current densities or applied potential, enhanced performance is witnessed due to the availability of both acid and alkaline reaction pathways, as shown through the perturbation analysis. However, at higher current densities transport dominates and the local pH rapidly drops at the electrode surface as shown via transport modeling. We determined that the local pH deviates significantly from the bulk pH for cases of intermediate pH, and decreases significantly near the anode. Additionally,

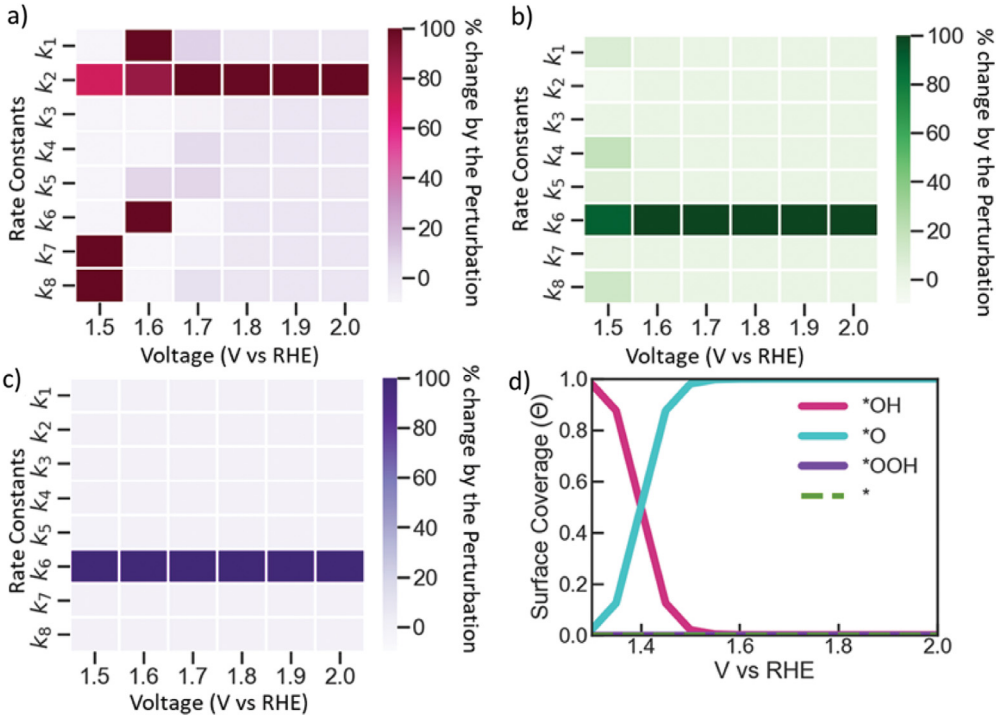

Fig. 5. The percent change in current density relative to that of the perturbation (0.1% change of the forward rate coefficient) on each of the eight forward rate coefficients at different applied potentials, 1.5 to 2 V vs. RHE, for a) pH 0, b) pH 9, and c) pH 13. 100% change represents that the overall current density (rate) changed by the same amount as that of the 0.1% perturbation. d) Surface coverage from 1.3 to 2.0 V vs. RHE for all pHs.

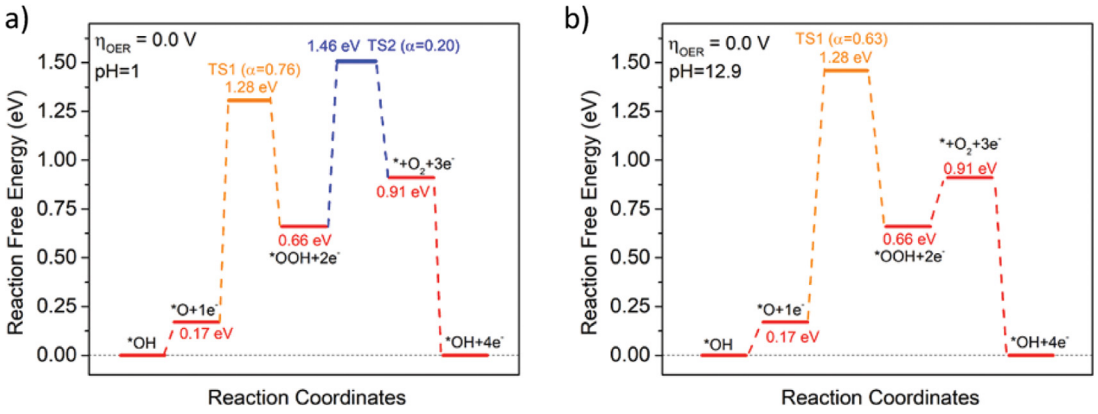

Fig. 6. OER free energy diagram in a) acidic and b) alkaline conditions at 0.0 V potential. α refers to the charge transfer coefficient of the individual elementary step ($0 < \alpha < 1$). To clarify the difference between α and β, we should note that the β refers to the overall charge transfer coefficient that reflects the degree of voltage effect on the free energy of TS. More details can be found in SI.

for low (1) and high (13) pH perform similarly at higher applied potentials and current densities. Through the perturbation analysis and evaluating the surface coverage, we show that there is only one rate determining step for the three pHs at these higher potentials. The findings of this paper will assist in designing more efficient electrochemical and photoelectrochemical systems that can address the transport limitations.

Declaration of competing interest

The authors have nothing to declare in terms of conflicts of interest.

Credit authorship contribution statement

Julie C. Fornaciari: Software, Validation, Investigation, Formal analysis, Writing – original draft, Writing – review & editing, Data curation, Visualization. **Lien-Chun Weng:** Methodology, Software, Validation, Data curation, Writing – review & editing. **Shaun M. Alia:** Investigation, Resources, Data curation, Writing – review & editing. **Cheng Zhan:** Writing – review & editing, Formal analysis, Software, Validation. **Tuan Anh Pham:** Writing – review & editing, Formal analysis. **Alexis T. Bell:** Writing – review & editing, Supervision. **Tadashi Ogitsu:** Writing – review & editing, Supervision, Project administration, Funding acquisition, Conceptualization. **Nemanja Danilovic:** Writing – review & editing, Supervision, Project administration, Conceptualization. **Adam Z. Weber:** Writing – review & editing, Supervision, Project administration, Funding acquisition, Conceptualization.

Acknowledgements

The authors acknowledge the HydroGen Energy Materials Network from the Department of Energy, Hydrogen and Fuel Cell

Technologies Office for funding under Contract numbers DE-AC02-05CH11231. Part of this work was performed under the auspices of the U.S. Department of Energy by Lawrence Livermore National Laboratory under Contract numbers DE-AC52-07NA27344 and the National Renewable Energy Laboratory under Contract numbers DE-AC36-08GO28308. JCF thanks the National Science Foundation (grant DGE 1106400) for support. The views expressed in the article do not necessarily represent the views of the DOE or the U.S. Government. The U.S. Government retains and the publisher, by accepting the article for publication, acknowledges that the U.S. Government retains a nonexclusive, paid-up, irrevocable, worldwide license to publish or reproduce the published form of this work, or allow others to do so, for U.S. Government purposes.

Supplementary materials

Supplementary material associated with this article can be found, in the online version, at doi:10.1016/j.electacta.2021.139810.

References

[1] H. Ahmad, S.K. Kamarudin, L.J. Minggu, M. Kassim, Hydrogen from photo-catalytic water splitting process: a review, Renew. Sustain. Energy Rev. 43 (2015) 599–610.
[2] S. Chu, A. Majumdar, Opportunities and challenges for a sustainable energy future, Nature 488 (2012) 294–303.
[3] S.P. Badwal, S.S. Giddey, C. Munnings, A.I. Bhatt, A.F. Hollenkamp, Emerging electrochemical energy conversion and storage technologies, Front. Chem. 2 (2014) 79.
[4] I. Dincer, C. Acar, Innovation in hydrogen production, Int. J. Hydrog. Energy 42 (2017) 14843–14864.
[5] S. Ardo, D. Fernandez Rivas, M.A. Modestino, V. Schulze Greiving, F.F. Abdi, E. Alarcon Llado, V. Artero, K. Ayers, C. Battaglia, J.-P. Becker, D. Bederak, A. Berger, F. Buda, E. Chinello, B. Dam, V. Di Palma, T. Edvinsson, K. Fujii, H. Gardeniers, H. Geerlings, S.M.H. Hashemi, S. Haussener, F. Houle, J. Huskens, B.D. James, K. Konrad, A. Kudo, P.P. Kunturu, D. Lohse, B. Mei, E.L. Miller, G.F. Moore, J. Muller, K.L. Orchard, T.E. Rosser, F.H. Saadi, J.-.W. Schüttauf, B. Seger, S.W. Sheehan, W.A. Smith, J. Spurgeon, M.H. Tang, R. van de Krol, P.C.K. Vesborg, P. Westerik, Pathways to electrochemical solar-hydrogen technologies, Energy Environ. Sci. 11 (2018) 2768–2783.
[6] M. Carmo, D.L. Fritz, J. Mergel, D. Stolten, A comprehensive review on PEM water electrolysis, Int. J. Hydrog. Energy 38 (2013) 4901–4934.
[7] N.T. Suen, S.F. Hung, Q. Quan, N. Zhang, Y.J. Xu, H.M. Chen, Electrocatalysis for the oxygen evolution reaction: recent development and future perspectives, Chem. Soc. Rev. 46 (2017) 337–365.
[8] M. Tahir, L. Pan, F. Idrees, X. Zhang, L. Wang, J.-J. Zou, Z.L. Wang, Electrocatalytic oxygen evolution reaction for energy conversion and storage: a comprehensive review, Nano Energy 37 (2017) 136–157.
[9] L. An, C. Wei, M. Lu, H. Liu, Y. Chen, G.G. Scherer, A.C. Fisher, P. Xi, Z.J. Xu, C.H. Yan, Recent development of oxygen evolution electrocatalysts in acidic environment, Adv. Mater. 33 (2021) e2006328.
[10] J.A. Arminio-Ravelo, A.W. Jensen, K.D. Jensen, J. Quinson, M. Escudero-Escribano, Electrolyte effects on the electrocatalytic performance of iridium-based nanoparticles for oxygen evolution in rotating disc electrodes, ChemPhysChem 20 (2019) 2956–2963.
[11] T. Reier, H.N. Nong, D. Teschner, R. Schlögl, P. Strasser, Electrocatalytic oxygen evolution reaction in acidic environments – reaction mechanisms and catalysts, Adv. Energy Mater. 7 (2017).
[12] T. Naito, T. Shinagawa, T. Nishimoto, K. Takanabe, Recent advances in understanding oxygen evolution reaction mechanisms over iridium oxide, Inorg. Chem. Front. 8 (2021) 2900–2917.
[13] C. Xiang, A.Z. Weber, S. Ardo, A. Berger, Y. Chen, R. Coridan, K.T. Fountaine, S. Haussener, S. Hu, R. Liu, N.S. Lewis, M.A. Modestino, M.M. Shaner, M.R. Singh, J.C. Stevens, K. Sun, K. Walczak, Modeling, simulation, and implementation of solar-driven water-splitting devices, Angew. Chem. Int. Ed Engl. 55 (2016) 12974–12988.
[14] T. Jafari, E. Moharreri, A.S. Amin, R. Miao, W. Song, S.L. Suib, Photocatalytic water splitting-the untamed dream: a review of recent advances, Molecules 21 (2016).
[15] T.A. Kistler, D. Larson, K. Walczak, P. Agbo, I.D. Sharp, A.Z. Weber, N. Danilovic, Integrated membrane-electrode-assembly photoelectrochemical cell under various feed conditions for solar water splitting, J. Electrochem. Soc. 166 (2018) H3020–H3028.
[16] D.K.D. Timothy, R.Cook, S.Y. Reece, Yogesh Surendranath, T.S. Teets, D.G. Nocera, Solar energy supply and storage for the legacy and nonlegacy worlds, Chem. Rev. 110 (2010) 6474–6502.
[17] A.W. Jensen, G.W. Sievers, K.D. Jensen, J. Quinson, J.A. Arminio-Ravelo, V. Brüser, M. Arenz, M. Escudero-Escribano, Self-supported nanostructured iridium-based networks as highly active electrocatalysts for oxygen evolution in acidic media, J. Mater. Chem. A 8 (2020) 1066–1071.
[18] S.M. Alia, B. Rasimick, C. Ngo, K.C. Neyerlin, S.S. Kocha, S. Pylypenko, H. Xu, B.S. Pivovar, Activity and durability of iridium nanoparticles in the oxygen evolution reaction, J. Electrochem. Soc. 163 (2016) F3105–F3112.
[19] S.M. Alia, G.C. Anderson, Iridium oxygen evolution activity and durability baselines in rotating disk electrode half-cells, J. Electrochem. Soc. 166 (2019) F282–F294.
[20] G.C. Anderson, B.S. Pivovar, S.M. Alia, Establishing performance baselines for the oxygen evolution reaction in alkaline electrolytes, J. Electrochem. Soc. 167 (2020).
[21] S. Ghoshal, B.S. Pivovar, S.M. Alia, Evaluating the effect of membrane-ionomer combinations and supporting electrolytes on the performance of cobalt nanoparticle anodes in anion exchange membrane electrolyzers, J. Power Sources 488 (2021).
[22] J. Liu, Z. Kang, D. Li, M. Pak, S.M. Alia, C. Fujimoto, G. Bender, Y.S. Kim, A.Z. Weber, Elucidating the role of hydroxide electrolyte on anion-exchange-membrane water electrolyzer performance, J. Electrochem. Soc. 168 (2021).
[23] C.F. Dickens, C. Kirk, J.K. Nørskov, Insights into the electrochemical oxygen evolution reaction with ab initio calculations and microkinetic modeling: beyond the limiting potential volcano, J. Phys. Chem. C 123 (2019) 18960–18977.
[24] H. Over, Surface chemistry of ruthenium dioxide in heterogeneous catalysis and electrocatalysis: from fundamental to applied research, Chem. Rev. 112 (2012) 3356–3426.
[25] T. Nishimoto, T. Shinagawa, T. Naito, K. Takanabe, Microkinetic assessment of electrocatalytic oxygen evolution reaction over iridium oxide in unbuffered conditions, J. Catal. 391 (2020) 435–445.
[26] M.R. Singh, J.D. Goodpaster, A.Z. Weber, M. Head-Gordon, A.T. Bell, Mechanistic insights into electrochemical reduction of CO2 over Ag using density functional theory and transport models, Proc. Natl. Acad. Sci. U. S. A. 114 (2017) E8812–E8821.
[27] D. Strmcnik, M. Uchimura, C. Wang, R. Subbaraman, N. Danilovic, D. Van Der Vliet, A.P. Paulikas, V.R. Stamenkovic, N.M. Markovic, in: Improving the Hydrogen Oxidation Reaction Rate By Promotion of Hydroxyl adsorption, Nature Chemistry, Nature Publishing Group, 2013, pp. 300–306.
[28] J. Rossmeisl, Z.-.W. Qu, H. Zhu, G.-.J. Kroes, J.K. Nørskov, Electrolysis of water on oxide surfaces, J. Electroanal. Chem. 607 (2007) 83–89.
[29] I.C. Man, H.Y. Su, F. Calle-Vallejo, H.A. Hansen, J.I. Martínez, N.G. Inoglu, J. Kitchin, T.F. Jaramillo, J.K. Nørskov, J. Rossmeisl, Universality in oxygen evolution electrocatalysis on oxide surfaces, ChemCatChem 3 (2011) 1159–1165.
[30] K.S. Exner, H. Over, Beyond the rate-determining step in the oxygen evolution reaction over a single-crystalline IrO2(110) model electrode: kinetic scaling relations, ACS Catal 9 (2019) 6755–6765.
[31] P. Giannozzi, S. Baroni, N. Bonini, M. Calandra, R. Car, C. Cavazzoni, D. Ceresoli, G.L. Chiarotti, M. Cococcioni, I. Dabo, A. Dal Corso, S. de Gironcoli, S. Fabris, G. Fratesi, R. Gebauer, U. Gerstmann, C. Gougoussis, A. Kokalj, M. Lazzeri, L. Martin-Samos, N. Marzari, F. Mauri, R. Mazzarello, S. Paolini, A. Pasquarello, L. Paulatto, C. Sbraccia, S. Scandolo, G. Sclauzero, A.P. Seitsonen, A. Smogunov, P. Umari, R.M. Wentzcovitch, QUANTUM ESPRESSO: a modular and open–source software project for quantum simulations of materials, J. Phys. Condens. Matter 21 (2009) 395502.
[32] K.B.J.P. Perdew, M. Ernzerhof, Generalized gradient approximation made simple, Phys. Rev. Lett. 77 (1996) 3865–3868.
[33] S. Grimme, Semiempirical GGA-type density functional constructed with a long-range dispersion correction, J. Comput. Chem. 27 (2006) 1787–1799.
[34] A.A. Peterson, F. Abild-Pedersen, F. Studt, J. Rossmeisl, J.K. Nørskov, How copper catalyzes the electroreduction of carbon dioxide into hydrocarbon fuels, Energy Environ. Sci. 3 (2010).
[35] Y. Lee, J. Suntivich, K.J. May, E.E. Perry, Y. Shao-Horn, Synthesis and activities of rutile IrO2 and RuO2 nanoparticles for oxygen evolution in acid and alkaline solutions, J. Phys. Chem. Lett. 3 (2012) 399–404.
[36] L. Giordano, B. Han, M. Risch, W.T. Hong, R.R. Rao, K.A. Stoerzinger, Y. Shao-Horn, pH dependence of OER activity of oxides: current and future perspectives, Catal. Today 262 (2016) 2–10.
[37] H. Hashiba, L.-.C. Weng, Y. Chen, H.K. Sato, S. Yotsuhashi, C. Xiang, A.Z. Weber, Effects of electrolyte buffer capacity on surface reactant species and the reaction rate of CO2 in electrochemical CO2 reduction, J. Phys. Chem. C 122 (2018) 3719–3726.
[38] Integrated Solar Fuel Generators, 2019.
[39] D.Y. Kuo, J.K. Kawasaki, J.N. Nelson, J. Kloppenburg, G. Hautier, K.M. Shen, D.G. Schlom, J. Suntivich, Influence of surface adsorption on the oxygen evolution reaction on IrO2(110), J. Am. Chem. Soc. 139 (2017) 3473–3479.
[40] S. Axnanda, E.J. Crumlin, B. Mao, S. Rani, R. Chang, P.G. Karlsson, M.O. Edwards, M. Lundqvist, R. Moberg, P. Ross, Z. Hussain, Z. Liu, Using "Tender" X-ray ambient pressure X-ray photoelectron spectroscopy as a direct probe of solid-liquid interface, Sci. Rep. 5 (2015) 9788.
[41] M. Favaro, H. Xiao, T. Cheng, W.A. Goddard 3rd, J. Yano, E.J. Crumlin, Subsurface oxide plays a critical role in CO2 activation by Cu(111) surfaces to form chemisorbed CO2, the first step in reduction of CO2, Proc. Natl. Acad. Sci. U. S. A. 114 (2017) 6706–6711.
[42] J. Qian, Y. Ye, H. Yang, J. Yano, E.J. Crumlin, W.A. Goddard 3rd, Initial steps in forming the electrode-electrolyte interface: H2O adsorption and complex formation on the Ag(111) surface from combining quantum mechanics calculations and ambient pressure X-ray photoelectron spectroscopy, J. Am. Chem. Soc. 141 (2019) 6946–6954.